In-depth analysis of the species and transformations during sol gel-assisted V_2PC synthesis

Jordan Sinclair[1], Marco Flores[1], Alexander M. Brugh[1], Tijana Rajh[1], Mikkel Juelsholt[3], Aysha A. Riaz[4] Christoph Schlueter[5], Anna Regoutz[4], and Christina S. Birkel[1,2*]

[1]School of Molecular Sciences, Arizona State University, Tempe AZ-85282, USA.

[2]Department of Chemistry and Biochemistry, Technische Universität Darmstadt, Darmstadt, Germany

[3]Department of Materials, University of Oxford, Parks Road, Oxford, OX1 3PH UK

[4] Department of Chemistry, University College London, 20 Gordon Street, London WC1H 0AJ, United Kingdom.

[5] Deutsches Elektronen-Synchrotron DESY, 22607 Hamburg, Germany.

KEYWORDS: MAX phase, sol-gel chemistry, V_2PC, mechanism, XRD, PDF, EPR, XPS, HAXPES

ABSTRACT: The sol-gel reaction mechanism of 211 MAX phases has proven to be very complex when identifying the intermediate species, chemical processes, and conversions that occur from a mixture of metal salts and gelling agent into a crystalline ternary carbide. With mostly qualitative results in the literature (Cr_2GaC, Cr_2GeC, and V_2GeC), additional analytical techniques, including thermal analysis, powder diffraction, total scattering and various spectroscopic methods, are necessary to unravel the identity of the chemical compounds and transformations during the reaction. Here, we demonstrate the combination of these techniques to understand the details of the sol-gel synthesis of MAX phase V_2PC. The metal phosphate complexes, as well as amorphous/nanocrystalline vanadium phosphate species (V in different oxidation states), are identified at all stages of the reaction and a full schematic of the reaction process is suggested. The early amorphous vanadium species undergo multiple changes of oxidation states while organic species decompose releasing a variety of small molecule gases. Amorphous oxides, analogous to $[NH_4][VO_2][HPO_4]$, V_2PO_4O, and $VO_2P_2O_7$ are identified in the dried gel obtained during the early stages of the heating process (300 and 600 °C), respectively. They are carbothermally reduced starting at 900 °C and subsequently react to crystalline V_2PC with the excess carbon in the reaction mixture. Through CHN analysis, we obtain an estimate of left-over amorphous carbon in the product which will guide future efforts of minimizing the amount of carbon in sol gel-produced MAX phases which is important for subsequent property studies.

Introduction

Solid state heating techniques have dominated the field of MAX phase synthesis since their initial preparation in the 1960s.[1,2] These methods have been manifested as the main synthesis techniques, even after their "revival" in 1996.[3–12] Solid state techniques include microwave heating, spark plasma sintering, isostatic hot pressing, and traditional furnace synthesis demonstrating a wide preparation portfolio. These methodologies, however, find limitations relative to wet chemical methods despite providing many avenues to receive MAX phases. The level of tunability offered by changing concentrations, pH, chelating strength, type of reagent or taking advantage of specific solution-based mechanisms is unmatched with wet chemical approaches. Sol gel chemistry is an example of a technique that utilizes all of these advantages. Discovered in 19th century[13], sol-gel synthesis routes have demonstrated large proficiency in developing inorganic materials, such as SiO_2, TiO_2, and even Eu- doped LuO_3 as a couple examples.[13–15] More specialized versions of the technique such as the Pechini method enabled synthesis of CeO_2, YBCO, and Ni_6Mo_6C by means of small molecules chelating ligands that generate homogenous solutions of metal/citrate complexes followed by production of a covalent polymer network that serves a trap for metal ions.[13]

For MAX phase synthesis – that historically is performed by solid state methods – a heavily modified version of the Pechini method, known as the amorphous metal complex method, has been developed. [16–22] This technique is based on alpha hydroxy carboxylic acids, like citric acid, that chelate metal ions and form metal complexes. This produces an amorphous gel-like matrix upon evaporation of solvent, and ultimately forms gels. This is different from the Pechini method that requires both alpha hydroxy carboxylic

acids and ethylene glycol.[13] The gels are heat treated to facilitate carbothermal reduction of the metal oxide phases and finally react into the carbide or carbonitride products. Carbothermal reduction is achieved by an excess of carbon that stems from the citric acid, which also acts as the carbon source for carbide/carbonitride formation.[18] Bulk samples produced by the amorphous metal complex method consist of high crystalline wt% of MAX phases, for example, Cr_2GaC, V_2PC, $V_2GeC_{1-x}N_x$ as well as left-over amorphous carbon.[16,21,22] Moreover, the ability to shape the target phases - which is not possible with classical solid-state methods - offers a lot of versatility to this synthesis as demonstrated for Cr_2GaC (hollow) microspheres, microwires and thick films.[23]

Lacking from the literature is a thorough study of the properties of MAX phases synthesized in this manner. A few studies discussing transport properties exist but are limited by the amorphous carbon content that is present in the end products and may influence the properties.[16,19,20] Beyond this specific aspect, there is a large degree of complexity that stems from the chemistries involved in sol-gel based processes. The identity of constituent gases released during heat treating of the gels, the structure of metal chelates that form in the sol, and the mechanism to reduce metal oxides to MAX phases are all examples of this. A first success in unravelling the reaction pathway was achieved for the sol-gel-based synthesis of Cr_2GaC.[18] By ex-situ X-ray and neutron diffraction studies including Pair Distribution Function analysis as well as thermogravimetric analysis, Siebert *et al.* showed that amorphous Cr/Ga oxide species form that are reduced by disordered graphite (stemming from the gel building agent), and eventually react with it to form the ternary carbide.

Building upon these general principles, we turn to a more exotic 211 MAX phase, V_2PC, that has also been synthesized by a sol-gel-based approach. The V-P-C system in general displays a great deal of complexity in its phase diagram with a number of ternary phases that exists aside the 211 MAX phase, for example $V_5P_{2.83}C_{0.5}$ V_3PC, V_4P_2C.[24] This is especially cumbersome to deal with when it comes to the solid-state reactions because there are not many parameters that can be changed relative wet chemistry. This system is a suitable candidate for the exploration of the reaction pathway as well as a detailed analysis of intermediate species. Knowing the nature of intermediates and how and when they react is crucial for extending this synthesis method to other MAX phases and even to compounds beyond this class of materials. Vanadium phosphate solution chemistry proves to be very complicated because vanadium has many stable oxidation states.[25–27] Therefore, it is imperative that a variety of analytical techniques are utilized to elucidate chemical and structural information.

Here, we unleash different spectroscopic, diffraction and thermogravimetric techniques to provide an in-depth view into the sol-gel-based synthesis of V_2PC. The V-P-O species that form early during the reaction are identified, and we present the quantification of amorphous carbon in the product. These insights are crucial for understanding the formation pathway, potential transfer to other compounds, and meaningful future discussions of the (functional) properties of MAX phases obtained based on sol-gel chemistry.

Materials and Methods

V_2PC was synthesized by an amorphous metal complex sol-gel-based approach. The stoichiometry of the *M* and *A* element within V_2PC were approximately around 2:1. The starting reagents ammonium metavanadate (Acros Organics, 99.5%, NH_4VO_3), and phosphoric acid (Beantown Chemical, 85 wt.%, H_3PO_4) were chosen because of their ease of solubility in water. To yield a target 250 mg bulk sample, 100 mL of a stock solution of 1.0231 M Phosphoric Acid was prepared. Subsequently, 0.4037 g (3.45 mmols, 2 eq.) of ammonium metavanadate were weighed out in air and transferred to a beaker with 5 mL of DI water. The solution turned yellow indicating that V^{5+} free ions are in solution. Additionally, 2.14 mL (2.20 mmols, 1 eq.) of 1.023 M Phosphoric Acid (please note an excess in P is needed for the most phase pure synthesis) were added to the beaker which made the solution turn from yellow to orange to a deep reddish color. The mixture was stirred vigorously using a magnetic stir bar. After a few minutes, 1.757 g (9.15 mmols, 5.3 eq) of citric acid (Alfa Aesar, 99+%) was added to the V-P solution and the temperature was increased to 140 °C (heating plate). After 10-15 mins the solution transitions through different colors from reddish, to a deep green color (indicative of V^{3+}), to blackish green, to a deep blue (indicative of V^{4+}). Based on what is discussed later in the EPR section, there is likely a coexistence of V^{3+} and V^{4+} states in the sol. Heating of the solution was continued until the majority of the solvent was evaporated, before the temperature was decreased to 80 °C. Subsequently, gelation occurred upon further heating and stirring of the sol for another 20-30 mins.

The viscous dark blue gel was transferred to an alumina boat and loaded into a fused silica tube (approximately 20 cm in length and 2.5 cm in diameter for the tube opening). It is imperative that one end of the tube is open and the other is closed while the open end of the tube faces the away from the direction that protective gas is introduced to the system setup. The tube was placed inside of a horizontal 3-zone tube furnace (Carbolite, model EST). UHP Ar was flowed into the

horizontal tube furnace and left to sufficiently purge the environment for 30 mins. The sample was heated to 950 °C with a heating rate of 2 °C per minute, kept at that temperature for 5 hours, and passively cooled to room temperature (inside the furnace). The silverish honeycomb-like product was recovered and ground with an agate mortar and pestle for further analysis. (Reference Fig. S1-S5 to observe the formation of metal chelates and potential polymerization steps in the sol.) Note that an excess of citric acid is required to guarantee the successful reduction of the intermediate oxide species that form. For ex-situ studies, reactions were concluded after heating at temperatures ranging from 200-950 °C. Different synthesis stages were studied, by isolating intermediate samples after heating at different temperatures, by various spectroscopic, thermogravimetric, and diffraction techniques.

Electron Paramagnetic Resonance (EPR) studies were performed at the EPR facility of Arizona State University. Continuous wave EPR spectra were recorded at 110K using a Bruker ELEXSYS E580 continuous wave X-band spectrometer (Bruker, Rheinstetten, Germany) equipped with a liquid nitrogen temperature control system (ER 4131VT). The magnetic field modulation frequency was 100 kHz with a field modulation amplitude of 0.5 mT peak-to-peak. The microwave power was 1 mW, the microwave frequency was 9.40 GHz and the sweep time was 84 seconds. The EPR spectrum of reduced vanadium phosphate was interpreted using a spin Hamiltonian, $\mathcal{H}$, containing the electron Zeeman interaction with the applied magnetic field $\mathbf{B_0}$ and the hyperfine coupling (hfc) interaction with the ^{51}V (I = 7/2) nucleus:[28]

$$\mathcal{H} = \beta_e \, \mathbf{S} \, . \, \boldsymbol{g} \, . \, \mathbf{B_0} + h \, \mathbf{S} \, . \, \boldsymbol{A} \, . \, \mathbf{I} \qquad (1)$$

where $\mathbf{S}$ is the electron spin operator, $\mathbf{I}$ is the nuclear spin operator of ^{51}V, $\boldsymbol{A}$ is the hfc tensor in frequency units, $\boldsymbol{g}$ is the electronic g-tensor, β_e is the electron magneton, and h is Planck's constant. The electron Zeeman interaction is anisotropic and depends on the relative orientation between the magnetic field and the molecular axes of the vanadium complex. The hfc interaction represents the interaction between the magnetic moment of the unpaired electron (V^{4+}, S = ½) and the magnetic moment of the ^{51}V nucleus.

To quantitatively compare experimental and simulated spectra, we divided the spectra into N intervals, i.e. we treated the spectrum as an N-dimensional vector $\boldsymbol{R}$. Each component R_j has the amplitude of the EPR signal at a magnetic field B_j, with j varying from 1 to N. The amplitudes of the experimental and simulated spectra were normalized so that the span between the maximum and minimum values of R_j is 1. We compared the calculated amplitudes R_j^{calc} of the signal with the observed values R_j defining a root-mean-square deviation σ by:

$$\sigma(p_1, p_2, \ldots, p_n) = \left[\sum_j (R_j^{calc}(p_1, p_2, \ldots, p_n) - R_j^{exp})^2/N\right]^{1/2} \qquad (2)$$

where the sums are over the N values of j, and p's are the fitting parameters that produced the calculated spectrum. For our simulations, N was set equal to 1024. The EPR spectra were simulated using EasySpin (v 5.2.35), a computational package developed by Stoll and Schweiger[29] and based on Matlab (The MathWorks, Natick, MA, USA). EasySpin calculates EPR resonance fields using the energies of the states of the spin system obtained by direct diagonalization of the spin Hamiltonian (see Eq. 1). The EPR fitting procedure used a Monte Carlo type iteration to minimize the root-mean-square deviation, σ (see Eq. 2) between measured and simulated spectra. We searched for the optimum values of the following parameters: the principal components of $\boldsymbol{g}$ (i.e. g_x, g_y, and g_z), the principal components of the hfc tensor $\boldsymbol{A}$ (i.e. A_x, A_y, and A_z) and the peak-to-peak linewidths (ΔB_x, ΔB_y, and ΔB_z).

Attenuated Total Reflection Fourier Transform Infrared (ATR-FTIR) spectroscopy was performed on a xerogel of the starting materials dried at 100 °C using a high-performance diamond Smart iTX FTIR spectrometer (Thermo Scientific). The sample was placed onto the sample stage and pressed with the swivel press to make sure there was optimal contact to the monolithic diamond crystal. The range of analysis was performed in the standard mid-infrared region of 4000-400 cm^{-1}.

Thermogravimetric Differential Thermal Analysis Mass Spectroscopy (TG-DTA-MS) was conducted on a Netzsch STA409 coupled with a MS IPI 3000 on a dried xerogel material. The measurement was done in SCAN mode where a mass spectrum (m/z) from 1-50 was taken The temperature profile started from 40 °C and heat was raised from 1200 °C at a rate of 10 C°/min with a constant flow of Ar gas ranging from 0.2-0.4 liters per min. This setup extracted 10-100x greater resolution and stability while allowing for determination of evolved gases during decomposition. Thermal analysis and Mass Spectroscopy were acquired in parallel of the sample comparative to tests run on an STA449 matched with a Netzsch MS Aeolos. (Fig. S8, in the supporting information)

Hard X-ray photoelectron spectroscopy (HAXPES) was used to characterize the chemical environments and oxidation states of samples calcined at 600 and 900 °C and data were collected at beamline P22 at PETRAIII,

German Electron Synchrotron DESY in Hamburg, Germany.[30] Attempts to characterize samples at temperatures of 100 and 300 °C were made but did not provide meaningful data due to excessive degassing in the UHV chambers. This agrees with the TG results showing major instabilities at low temperatures. A photon energy of 6 keV was used for all experiments, with the energy selected using a Si (111) double-crystal monochromator. A Phoibos 225HV analyzer (SPECS, Berlin, Germany) was used with the small area lens mode and a slit size of 3 mm. Spectra were collected using a pass energy of 30 eV. The total energy resolution in this setup was determined to be 245 meV, the 16/84% Fermi edge (E_F) width of a polycrystalline gold foil, and all spectra were aligned to the Au E_F. All samples were mounted as received on conductive carbon tape.

For X-ray diffraction (XRD) analysis, all synthesized products were ground with an agate mortar pestle and mounted onto a flat cylindrical Si low background stage. The X-ray powder diffractograms were generated and recorded using a Bruker D2 Phaser (2nd Generation) powder X-ray diffractometer that utilizes Ni-filtered Cu Kα radiation (λ = 1.5406). Data collection was performed at room temperature with 2θ ranges extending from 10°-90° and a step size of 0.05°. The experimentally generated diffractograms were matched with theoretical profiles and patterns to determine present phases. Analysis of the Bragg peaks and percentages of existing phases were carried out using a Rietveld refinement with the assistance of Topas.[31]

For the CHN (carbon, hydrogen, nitrogen) analysis, 1-1.5 mg of the V_2PC target phase were taken from a sample batch 4 times to make sure all parts of the sample exhibit similar content and were mixed with 0.4-2.8 mg of combustion aid WO_3. The combustion aid was varied to ensure the complete combustion of the crystalline samples. All four mixed samples were placed in tin cups and folded to ensure sample compactness. The samples were then loaded into a PE 2400 and were flash combusted at a temperature of 1760 °C. Detection of the total C, H, and N content is conducted by a thermal conductivity detector with precision up to 0.1 g.

Total scattering data were collected at Deutsches Elektronen Synchrotron (DESY), Hamburg, Germany at beamline P02.1. The samples were loaded into a 1 mm Kapton capillary and measured with a wavelength of λ = 0.2071 Å. The X-ray Pair Distribution Functions (PDFs) were obtained utilizing PDFgetX3[32] in XPDFsuite.[33] The X-ray scattering signal from an empty Kapton tube was used for background subtraction. The X-ray PDF of crystalline V_2PC was refined using PDFgui.[34] The refinement for V_2PC converged the unit cell parameters, isotropic atomic displacement parameters, scale factor, and atomic positions to reasonable values. The crystallite size was explained by spherical dampening using a parameter known as the
SP diameter. The V_2PC refinement was carried out with the space group $P6_3/mmc$.
Analysis of the microstructure was done using an Auriga-Zeiss FIB SEM. (See Fig. S9-10) The composition of the samples was identified making use of an Oxford Instruments SDD detector (Ultim MAX). A standard aluminum stage holder was covered with carbon tape to fix powders to the holder surface. The beam current was set at a 20 keV accelerating potential primarily for the EDS that was conducted. Multiple sites of the bulk samples were analyzed at varying magnifications.

Results and Discussion

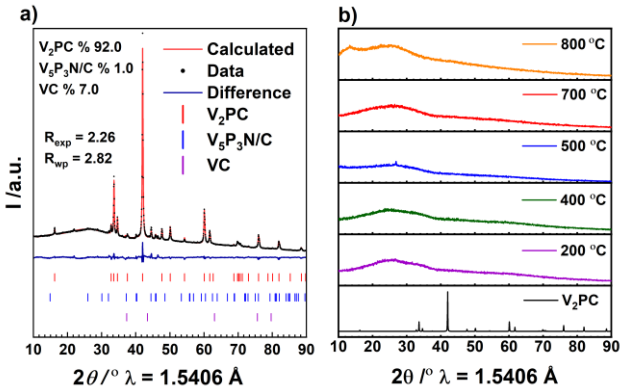

Figure 1: (a) Rietveld refinement of the XRD data of the V_2PC crystalline product obtained at 950 °C. (b) PXRD data of samples heat treated at different temperatures.

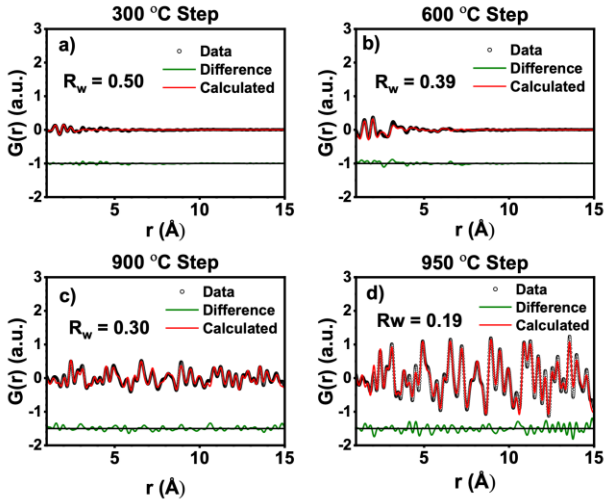

Figure 2: PDF analysis of the total scattering data of the samples collected at (a) 300 °C (b) 600 °C (c) 900 °C (d) 950°C.

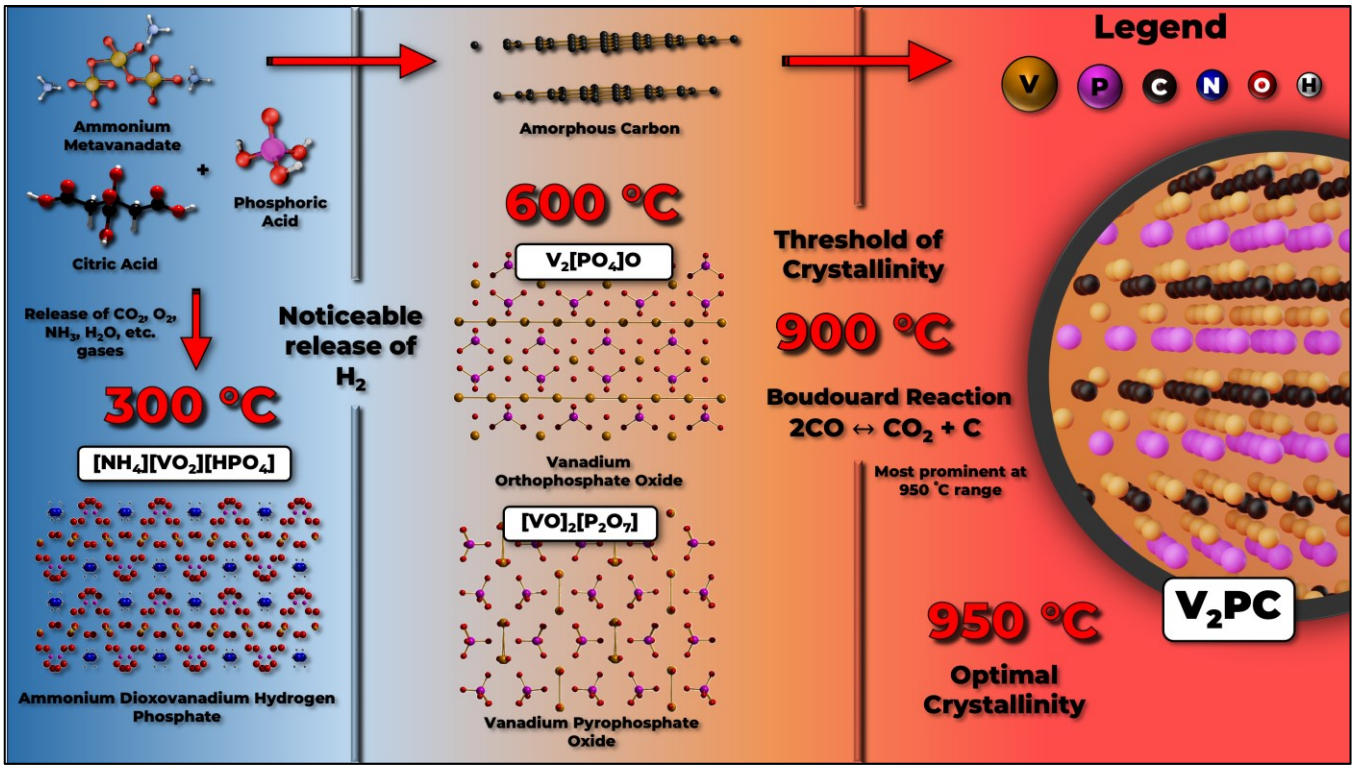

Figure 3: A schematic of all species identified when mixing the starting reagents and heating all the way to the max temperature of 950 °C. Please note that the structure of the amorphous carbon that is a part of the reaction mixture and participates in the reaction at high temperatures has been structurally described in reference[18].

X-ray powder diffraction data were collected on samples synthesized at temperatures between 200 and 950 °C (Fig. 1). Samples prepared at temperatures of and below 800 °C do not show any Bragg peaks in the (laboratory) XRD data, indicating that no long-range order exists (Fig. 1 b and Table S2). The sample processed at 950 °C, however, exhibits sharp Bragg peaks (Fig. 1 a) that can be assigned to three crystalline phases, MAX phase V_2PC and two minor side phases V_5P_3N/C and VC. Note that the obtained weight % of the side phases can vary slightly from synthesis to synthesis, but the MAX phase is always at least 92 wt%.[2,21] Since the laboratory X-ray diffraction measurements of the samples produced at 800 °C and below did not provide useful information for identifying the intermediate species, beamline diffraction data were obtained for samples collected at 300 °C, 600 °C, 900 °C and 950 °C, respectively (Fig. 2). These temperatures were chosen because the samples obtained at these temperatures most efficiently capture the intermediate species as well as the onset of the formation of the target MAX phase and the optimized synthesis temperature. PDF analysis of these data show that the crystallinity of the sample increases with increasing temperature and that long-range order sets in at a synthesis temperature of about 900 °C.

The V-O-P species in the sample obtained at 300 °C can be described as nanostructured $[NH_4][VO_2][HPO_4]$ along with some amount of nanostructured V_2PO_4O. However, since the structural coherence length (crystallite size) is smaller than the unit cells of $[NH_4][VO_2][HPO_4]$ and V_2PO_4O the sample obtained at 300 °C does not contain these crystal structures. Instead, this suggests that the species at this stage contain the same types of coordination and bonds as $[NH_4][VO_2][HPO_4]$ and V_2PO_4O. Fitting the compounds separately to the collected data at a temperature of 300 °C yields R_w values of 0.85 and 0.78 for $[NH_4][VO_2][HPO_4]$ and V_2PO_4O, respectively (see Fig. S11). Incorporating both structures into a refinement decreases the R_w to 0.50, as shown in Figure 2 (a). At higher r-values, the fit can be improved as only a simple spherical size dampening model is applied. However, as we are mostly interested in the chemical nature of the sample, a better description of the size distribution and longer-range molecular packing is beyond the scope of this paper. Between 300 and 600 °C, all compounds are oxidized further and models of a mixture of nanocrystalline V_2PO_4O and $VO_2P_2O_7$ give a good description of the experimental PDF, as shown in Figure 2 (b). This is further corroborated by the HAXPES data, which describe PO_4/P_2O_7 and V-O bonding environments at 600 °C, which is further analyzed in greater detail later on. (Preliminary models of these PDF fits are shown Fig. S12.) Further heating to 900 °C leads to the formation of the crystalline phases VC,

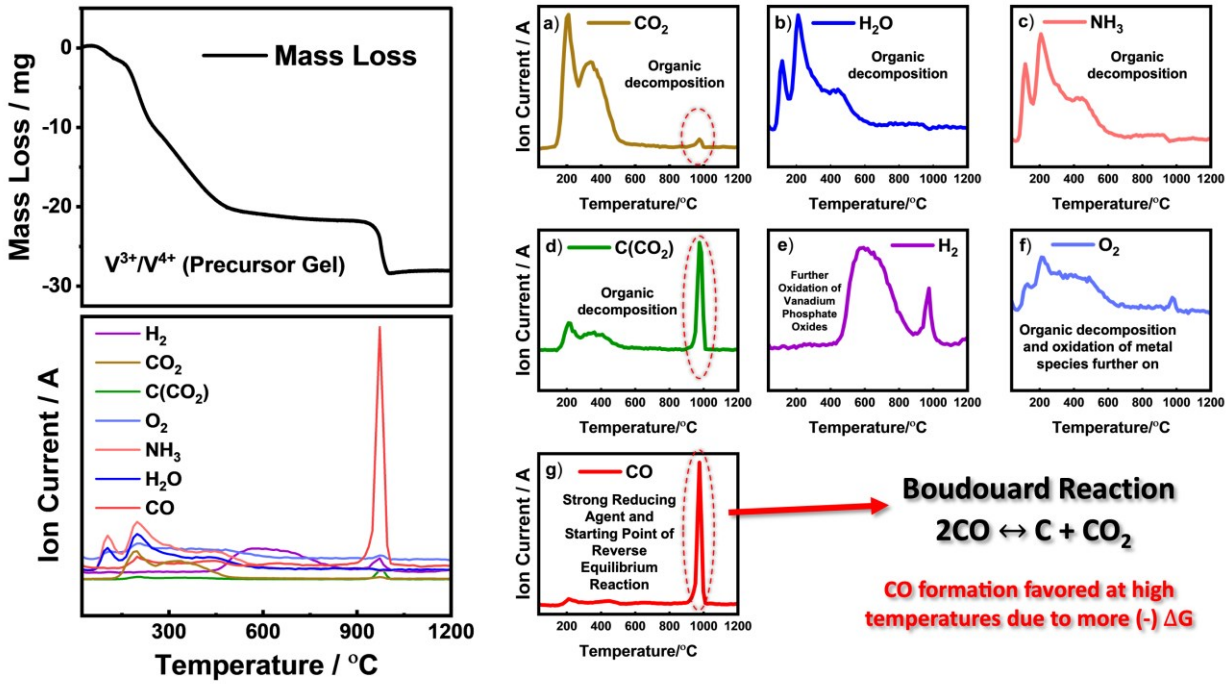

Figure 4: TG-Single Scan MS of a V_2PC sample across 40-1200 °C (a) CO_2 scan (b) H_2O scan (c) NH_3 scan (d) C scan (e) H_2 scan (f) O_2 scan (g) CO scan.

V_5P_3N/C, and V_2PC which fit well to the PDF, R_w of 0.30 Figure 2 (c). (See Figure S15 for more insight) Finally, at 950 °C, the same phases are present with larger crystallite size and verified by standard XRD, Figure S14, and again in Figure 1 (a) by Rietveld refinement (refer to Table S3-S33) for PDF refinement data). Please note that PDF analysis (Figure 2) only includes the V-P-O species and not the carbon species present. Based on our earlier works on the sol gel-based synthesis of Cr_2GaC[18], we know from neutron diffraction experiments that an excess of carbon exists in the form of disordered nanostructured graphite (after decomposition of the citric acid) until it participates in the reaction starting at around 900 °C. Figure 3 shows a schematic of all species identified from start to finish. The product can be washed with acid to remove most of the side phases.[21] This however does not apply to the amorphous carbon species, which cannot be removed by acid wash, and it is not detectable by laboratory XRD analysis. Visually in Figure 1(a) there is a large broadening of the PXRD pattern within the 2θ range that could be indicative of amorphous carbon (See Table S34 for Rietveld refinement data). Note that an excess of carbon is used (citric acid) to ensure reduction of oxides and subsequent reaction into the carbide MAX phase. More analytical processing through use of CHN-analysis was performed to address the appearance of this broadening in later sections.

Following the chemical process by TG-DTA-MS, there are a couple points that garner attention. In the temperature ranges of 175-225 °C, the decomposition of all reduced vanadium phosphate organic species is observed. The constituent gases evolving off most prevalently in this region are identified as CO_2 and H_2O as shown in Figure 4 and S8. Regarding the gases that were more difficult to discern such as NH_3 and O_2, TG-Single Scan MS measurements on the MS IPI 3000 were performed to correctly assign all the gases as seen in Figure 4. Dialing in at approximately 400 °C, a conversion of citric acid to a carbon species is observed. The m/z ratios attributed to Figure 4, panel (d) correspond to that of 12. This is easy to rationalize as a C fragment results from the large productions of CO_2/CO from the Boudouard reaction.[18] CO_2 dominants the equilibrium of the reaction at low temperatures because it possesses a lower (more negative) formation entropy relative to CO. Due to formation entropy always having temperature dependence and the formation entropy of CO_2 being sufficiently low, the Gibbs free energy of CO_2 is almost a constant. The opposite holds true for the Gibbs Free energy of CO which is still dependent on temperature. so, the equilibrium at lower temperatures will not favor it. These ideas are validated more in the TG-Single Spectra-MS (Fig. 4), TG-DTA-MS data (Fig. S8), and is also the case in similar works.[18] At around 575-750 °C, an appreciable amount of H_2 gas is generated. This indicates there is a release of this gas following the further oxidation

of the vanadium phosphate oxide species. Further along, at approximately 950 °C, H_2 gas and a large amount of CO is produced (notable reducing agent). This outgassing of CO aligns again with principles of the Boudouard reaction, where the chemical equilibrium between CO_2 and CO acts as a driving force for carbothermal reduction.[35]

$$2CO \leftrightarrow C + CO_2 \quad (3)$$

With the reaction profile reaching a maximum of 950 °C, the temperature is sufficient to drive the equilibrium reaction in the reverse direction, stimulating the large abundance of CO.[35] It can also be argued there is a small contribution of reduction from the generated H_2 but not to the degree of the enormous amounts of CO relative to the other constituent gases. The reduction of the metal V-P oxides is followed by reaction

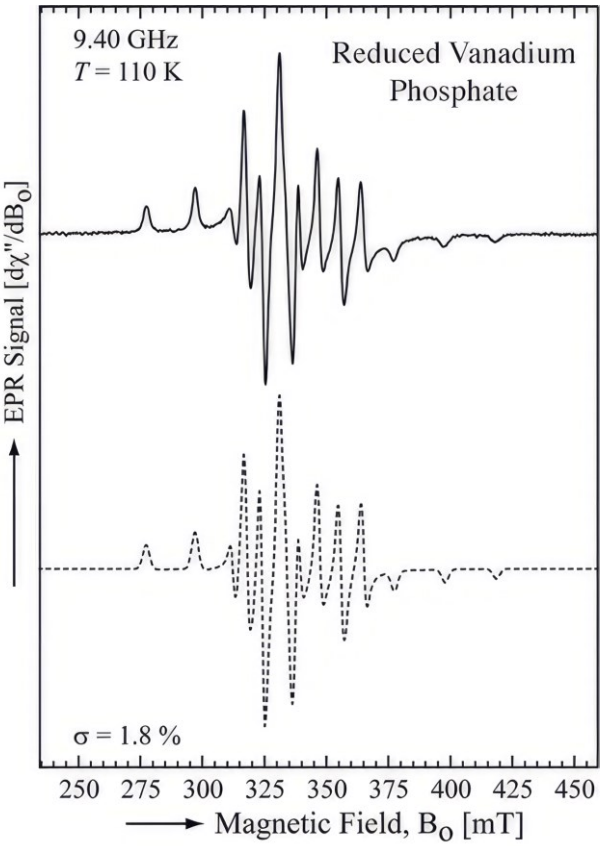

Figure 5: Experimental (solid line) and simulated (dashed line) X-band EPR spectra of reduced vanadium phosphate at 110 K.

with amorphous carbon to produce the MAX phase product (also see Figure 3).

To further shed light on the identity of the intermedia te vanadium phosphate species in the sol during sol-gel mixing and heating, several spectroscopy techniques were utilized. Figure 5 shows the X-band (9.40 GHz) electron paramagnetic resonance (EPR) spectrum of reduced vanadium phosphate, intermediary of the V_2PC sol-gel reaction ("sol"-phase), recorded at 110 K. Although a signal consistent with the presence of V^{4+} was observed (Fig. 5, solid line), the spin state of the metal center and its hyperfine coupling interaction could not be determined by simple inspection of the spectrum. To obtain the EPR parameters, the respective spin Hamiltonian was fit to the data (Fig. 5, dashed line). The spectral features observed for reduced vanadium phosphate were well-fit (σ = 1.8%, see Materials and Methods) considering a $^{51}V^{4+}$ center (S = 1/2, I = 7/2) with nearly axial g values and axial hyperfine couplings (see Table 1). Furthermore, a spin-counting experiment was also performed to determine the quantity of V^{4+} present in a solution of reduced vanadium phosphate relative to an equimolar solution of vanadyl acetylacetonate (100% in the V^{4+} state) using the same tube and settings. Comparison of the total double integrals revealed that the sample of reduced vanadium phosphate possessed only 46% of the V^{4+} present in the sample of vanadyl acetylacetonate. Consequently, it cannot be ruled out that the sample of reduced vanadium phosphate may contain a mix of V^{5+}, V^{4+} and V^{3+}. A remaining fraction of the initial state (V^{5+}) cannot be observed by EPR since it is diamagnetic. Whereas the state resulting from a two-electron reduction (V^{3+}) is EPR-silent at 9.40 GHz, i.e. no resonances would be detected using a conventional X-band spectrometer as the one used in this work.[36]

Table 1. Parameters used to fit the X-band EPR spectrum of reduced vanadium phosphate in the sol (at low temperature)

Parameter[a]	Reduced Vanadium Phosphate (T = 110 K)
g_x	1.977
g_y	1.972
g_z	1.929
$\|A_x\|$ (MHz)	205.5
$\|A_y\|$ (MHz)	190.8
$\|A_z\|$ (MHz)	544.8
ΔB_x (MHz)	53
ΔB_y (MHz)	107
ΔB_z (MHz)	85

[a] The fitting parameters were the following: the principal components of $\boldsymbol{g}$ (i.e. g_x, g_y, g_z,), the principal components of the hfc tensor $\boldsymbol{A}$ (i.e. A_x, A_y, and A_z) and the peak-to-peak line widths (ΔB_x, ΔB_y, and ΔB_z).

HAXPES experiments were conducted on two samples calcined at 600 and 900°C. The survey spectra (see Supplementary Information) show all expected core levels and a minute contribution from N 1*s*. All core level spectra in Figure 6 are normalized to their

respective total P 2*s* area. The lower temperature sample is dominated by oxygen-containing environments. The O 1*s* and V 2*p* core lines are close in binding energy and shown in Figure 6 (a). An intense oxygen signal is observed at a binding energy (BE) of 531.7 eV commensurate with PO_4/P_2O_7 environments. In addition to this, the spectra show low-intensity shoulders on both the lower and higher BE sides. A higher BE feature at approx. 533.2 eV fits the presence of PO_3/P_2O_5 environments, whilst the lower BE feature at approx. 530.6 eV stems from V-O environments. When going from 600 to 900°C, the largest decrease is observed for the PO_4/P_2O_7 environments, matching observations from PDF analysis in Figure 2. The V 2*p* lines for the 600°C sample show a single broad feature at a BE typical of oxidized vanadium in the +4 oxidation state (V $2p_{3/2}$ 516.3 eV).[37,38] At the higher temperature of 900°C, this environment diminishes, and the spectrum is dominated by a sharper feature at 513.2 eV associated with V-P and V-C environments. The C and P spectra also show the appearance of these environments only at the higher temperature. The C 1*s* core level spectra (see Fig. 6(b)) are dominated by adventitious/graphitic carbon species at 284.8 eV. This is expected because of the remaining amorphous carbon in the product. The asymmetric tail towards the higher BE (marked with an asterisk) could stem from both the graphitic nature of the C or from oxidized species. The C-V environments occur at a BE of 282.9 eV. HAXPES allows access to deeper core states and this was exploited in the case of phosphorous, where both the P 2*s* as well as the deep P 1*s* core level were collected (see Fig. 6 (c) and (d)). Both core levels show the same chemical environments with a higher BE feature from P-O environments in both samples (at 191.2 eV in the 2*s* and 2148.1 eV in the 1*s* spectrum) and a lower BE feature from P-V environments only in the 900°C sample (at 186.7 eV in the 2*s* and 2142.2 eV in the 1*s* spectrum). Due to the difference in kinetic energy, the probing depth changes between core levels and allows a non-destructive depth profile of a sample. In the present case, the probing depth is approximately a third higher for the P 2*s* (23.3 nm) compared to the P 1*s* (16.6 nm), meaning that the P 1*s* is more surface sensitive (the inelastic mean free paths for V_2PC were modelled using the QUASES-IMFP-TPP2M Ver.3.0 software package).[39] The ratio between the P-V and P-O states in the 900 °C sample changes only marginally, suggesting that on the probed length scales, the sample is homogeneous. Finally, the N 1*s* spectra (see Supplementary Information) decrease considerably in intensity (relative to P) upon an increase in the calcination temperature. The 600°C sample shows several NH_x environments between 399-401 eV, and the 900°C sample shows a narrow, well-defined peak at 397.9 eV commensurate with metal nitride environments. (See Fig. S6-S7 for additional information on the HAXPES spectra)

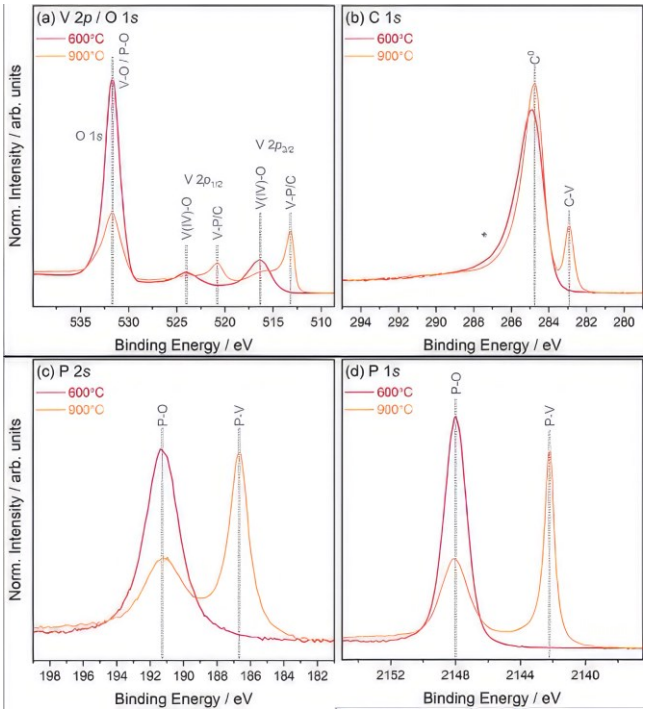

Figure 6: HAXPES core level spectra of the samples calcined at 600 and 900°C, including (a) V 2*p* and O 1*s*, (b) C 1*s*, (c) P 2*s*, and (d) P 1*s*. All spectra are normalized to their respective total P 2*s* area.

Turning more focus again toward the species in the sol-based steps of the synthesis. When mixing the starting reagents NH_4VO_3 and H_3PO_4 (V and P sources), drying them, and taking PXRD, a mixture of ammonium vanadium hydrogen oxide phosphate (NH_4HVPO_6) and ammonium vanadyl hydrogen phosphate (NH_4)(VO_2)(HPO_4) crystallize, as seen in Figure S13. The addition of citric acid, displayed in Figure S1 begins the reduction, chelation, and polymerization process of the vanadium phosphate species in the sol. The mechanism describing the formation of the ammonium vanadyl phosphates and their polymerization into a gel network is poorly understood.[40] A proposed mechanism for the metal ion chelation of the metavanadate ion is presented in Figure S2. It remains unclear whether the addition of citric acid polymerizes the ammonium vanadyl phosphate species as a whole, the polymerization is undergone separately for the metavanadate and phosphate groups, or if the ammonium vanadyl phosphate species sits entrapped in a gel-like network as would be expected for the amorphous metal complex technique. (see Figure S3 and S5) The last case is the most likely occurrence, but will need further exploration of the sol in future works.

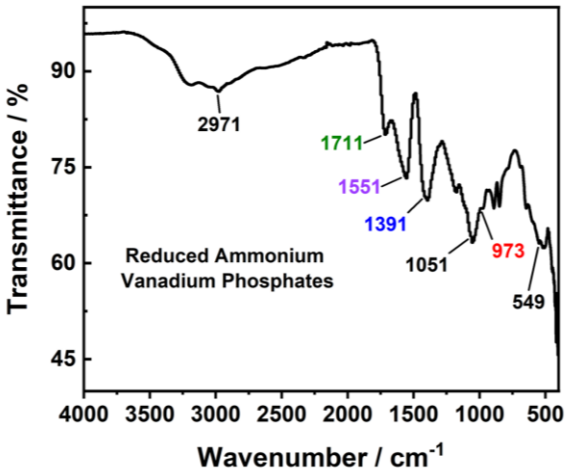

Atom Groupings	(Lit.) (cm^{-1})	(Exp.) (cm^{-1})
O-H stretch	3300-2500 [41]	2971
C=O stretch (carboxylic acid)	1725-1700 [41]	1711
Carboxylate Ion	1610-1550 [41]	1551
Ammonium Ion	1430-1390 [41]	1391
V=O stretch	Approx. 990 [42]	973
O-P-O deformation bend	1080-1022 [43]	1051
P-O asymmetric stretch	562-500 [43]	549

Figure 7: ATR-FTIR spectrum of reduced vanadium phosphates in the xerogel of mixed starting reagents. The xerogel was dried at 100 °C. Proposed sol-gel intermediate IR modes (color coded in the ATR-FTIR Plot).

The ATR-FTIR data (Fig. 7) confirms the presence of standard bending, stretching, and deformation modes of functional groups that comprise the proposed intermediate species. We find stretching/bending modes indicative of carboxylic acids in the range of 3300-2500 cm^{-1}.[41,42] The expected V=O stretching vibration at approximately 990[42] cm^{-1} shows up at 973 cm^{-1}. Phosphate O-P-O deformation bends and P-O asymmetric stretches are present in the ranges of 1080-1022[43] cm^{-1} and 562-500[43] cm^{-1} respectively. Ammonium ion bands also show up in the range of 1430-1390 cm^{-1}.[41] Tabulated ATR-FTIR data for most bending stretching, and deformations mode are displayed in Figure 7 and the remaining in Table S1. These again supplement that all the expected functional groups/species are there but are not definitive in concluding that these intermediates are as proposed in Figure 7.

CHN analysis was conducted on different batches of the final MAX phase V_2PC obtained at 950 °C in order to discuss the amount of (amorphous) carbon in the product. All samples yield a total of 17 % total carbon. Considering the target phase should only yield approximately 8% total carbon, the 17% also includes the side phase contribution along with the amorphous carbon that is present, commensurate with the HAXPES results showing a large contribution from adventitious carbon species. Note that there is a need for excess carbon to provide ample reducing power of oxides, as discussed in the experimental section. However, at this point, the quantification of the amount of "extra" carbon in the system is necessary for future works where the amount will be varied.

Table 2. Tabulated CHN analysis data of V_2PC sol-gel samples.

Sample	%C	%H	%N
1	17.1	0.90	0.56
2	17.1	0.75	0.55
3	17.2	0.83	0.56
4	17.2	0.87	0.51

Conclusion

The formation mechanism of MAX phase V_2PC via sol-gel-based reaction has been explored in great depth utilizing a combination of spectroscopic, diffraction and thermal analysis techniques (ATR-FTIR, EPR, HAXPES, TG-DTA-MS, PDF, PXRD). Generally, the reaction is a combination of a carbothermal reduction of amorphous oxygen-containing species (as shown for other MAX phases) followed by reaction with excess carbon to form the V_2PC product. The detailed analyses discussed here give detailed insights into the chemical composition, structure, and oxidation states of the involved elements, particularly of the intermediate (amorphous) species. The complexes present in the dried gel at the very beginning of the reaction are identified by spectroscopy. Amorphous oxides, analogous to $[NH_4][VO_2][HPO_4]$, V_2PO_4O, and $VO_2P_2O_7$ are identified in the dried gel obtained during the early stages of the heating process (300 and 600 °C), respectively. Crystalline phases are observed after treatment at around 900 °C. The sample experiences the biggest mass loss at temperatures below ~500 °C coinciding with gaseous CO_2, H_2O, and NH_3 leaving the reaction mixture. The onset of MAX phase formation is also

clearly visible with a spike in the CO signal at around 900 °C. To address the remaining amorphous carbon in the product, CHN analysis was performed. This is a crucial step towards understanding the properties of carbonaceous MAX phases produced by sol-gel chemistry as well as tuning (minimizing) the amount of carbon in the products.

ASSOCIATED CONTENT

Supporting Information

The Supporting Information. Additional experimental details, including reaction schemes/mechanisms, XRD data, and Rietveld refinement tables, TG-DTA-MS, HAXPES data, SEM, and PDF refinements/preliminary models. (.pdf)

AUTHOR INFORMATION

Corresponding Author

*christina.birkel@asu.edu

Author Contributions

J. Sinclair synthesized, analyzed the samples, and wrote the manuscript. A. Brugh prepared EPR samples. M. Flores performed EPR experiments and data analysis. M. Steinbrück performed TG-DTA-MS. M. Juelsholt performed the synchrotron XRD measurements and assisted in the total scattering analysis. AAR, CS and AR performed the HAXPES experiments and data analysis. C. S. Birkel provided the research question, wrote and reviewed the manuscript.

Funding Sources

This material is based upon work supported by the National Science Foundation under Grant No. 2143982. A.A.R acknowledges the support from the Department of Chemistry, UCL. A.R. acknowledges support from the Analytical Chemistry Trust Fund for her CAMS-UK Fellowship.

ACKNOWLEDGMENT

We acknowledge DESY (Hamburg, Germany), a member of the Helmholtz Association HGF, for the provision of experimental facilities. Parts of this research were carried out at PETRA III using beamline P22. Beamtime was allocated for proposal I-20221270. Parts of this research were carried out at PETRA III using beamline P02.1. AR acknowledges the support from the Institute of Physics (IOP) carer's fund, which provided financial support to enable her to attend the HAXPES experiments at PETRA III in person. The authors acknowledge the use of facilities within the Eyring Materials Center at Arizona State University, supported in part by NNCI-ECCS-1542160.

REFERENCES

(1) Von Kudielka, H. Strukturuntersuchungen an Carbosulfiden von Titan Und Zirkon. *Zeitschrift fur Kristallographie - New Crystal Structures* **1960**, *114* (1–6), 447–456. https://doi.org/10.1524/zkri.1960.114.1-6.447.

(2) Nowotny, H.; Jeitschko, W.; Goretzki, H. Die Kristallstruktur Yon V_2PC Und VsP_3N. *Monatsh Chem* **1968**, *99*, 672–675.

(3) Barsoum, M. W.; El-Raghy, T. Synthesis and Characterization of a Remarkable Ceramic: Ti_3SiC_2. *Journal of the American Ceramic Society* **1996**, *79* (7), 1953–1956. https://doi.org/10.1111/j.1151-2916.1996.tb08018.x.

(4) Sokol, M.; Natu, V.; Kota, S.; Barsoum, M. W. On the Chemical Diversity of the MAX Phases. *Trends Chem* **2019**, *1* (2), 210–223. https://doi.org/10.1016/j.trechm.2019.02.016.

(5) Chen, K.; Bai, X.; Mu, X.; Yan, P.; Qiu, N.; Li, Y.; Zhou, J.; Song, Y.; Zhang, Y.; Du, S.; Chai, Z.; Huang, Q. MAX Phase Zr_2SeC and Its Thermal Conduction Behavior. *J Eur Ceram Soc* **2021**, *41* (8), 4447–4451. https://doi.org/10.1016/j.jeurceram-soc.2021.03.013.

(6) Etzkorn, J.; Ade, M.; Kotzott, D.; Kleczek, M.; Hillebrecht, H. Ti_2GaC, Ti_4GaC_3 and Cr_2GaC-Synthesis, Crystal Growth and Structure Analysis of Ga-Containing MAX-Phases $M_{n+1}GaC_n$ with M = Ti, Cr and N = 1, 3. *J Solid State Chem* **2009**, *182* (5), 995–1002. https://doi.org/10.1016/j.jssc.2009.01.003.

(7) Wang, X.; Chen, K.; Wu, E.; Zhang, Y.; Ding, H.; Qiu, N.; Song, Y.; Du, S.; Chai, Z.; Huang, Q. Synthesis and Thermal Expansion of Chalcogenide MAX Phase Hf_2SeC. *J Eur Ceram Soc* **2022**, *42* (5), 2084–2088. https://doi.org/10.1016/j.jeurceramsoc.2021.12.062.

(8) Chirica, I. M.; Mirea, A. G.; Neaţu, Ş.; Florea, M.; Barsoum, M. W.; Neaţu, F. Applications of MAX Phases and MXenes as Catalysts. *J Mater Chem A Mater* **2021**, *9* (35), 19589–19612. https://doi.org/10.1039/d1ta04097a.

(9) Radovic, M.; Barsoum, M. W. MAX Phases: Bridging the Gap between Metals and Ceramics. *American Ceramic Society Bulletin* **2013**, *92* (3), 20–27.

(10) Wang, Z.; Ma, G.; Liu, L.; Wang, L.; Ke, P.; Xue, Q.; Wang, A. High-Performance Cr_2AlC MAX Phase Coatings: Oxidation Mechanisms in the 900–1100°C Temperature Range. *Corros Sci* **2020**, *167* (December 2019). https://doi.org/10.1016/j.corsci.2020.108492.

(11) Alnoor, H.; Elsukova, A.; Palisaitis, J.; Persson, I.; Tseng, E. N.; Lu, J.; Hultman, L.; Persson, P. O. Å. Exploring MXenes and Their MAX Phase Precursors by Electron Microscopy. *Mater Today Adv* **2021**, *9*. https://doi.org/10.1016/j.mtadv.2020.100123.

(12) Khazaei, M.; Ranjbar, A.; Esfarjani, K.; Bogdanovski, D.; Dronskowski, R.; Yunoki, S. Insights into Exfoliation Possibility of MAX Phases to MXenes. *Physical Chemistry Chemical Physics* **2018**, *20* (13), 8579–8592. https://doi.org/10.1039/c7cp08645h.

(13) Danks, A. E.; Hall, S. R.; Schnepp, Z. The Evolution of "Sol-Gel" Chemistry as a Technique for Materials Synthesis. *Mater Horiz* **2016**, *3* (2), 91–112. https://doi.org/10.1039/c5mh00260e.

(14) Dubey, R. S.; Rajesh, Y. B. R. D.; More, M. A. Synthesis and Characterization of SiO_2 Nanoparticles via Sol-Gel Method for Industrial Applications. In *Materials Today: Proceedings*; Elsevier Ltd, 2015; Vol. 2, pp 3575–3579. https://doi.org/10.1016/j.matpr.2015.07.098.

(15) Liang, Y.; Sun, S.; Deng, T.; Ding, H.; Chen, W.; Chen, Y. The Preparation of TiO_2 Film by the Sol-Gel Method and Evaluation of Its Self-Cleaning Property. *Materials* **2018**, *11* (3). https://doi.org/10.3390/ma11030450.

(16) Siebert, J. P.; Bischoff, L.; Lepple, M.; Zintler, A.; Molina-Luna, L.; Wiedwald, U.; Birkel, C. S. Sol-Gel Based Synthesis and Enhanced Processability of MAX Phase Cr_2GaC. *J Mater Chem C Mater* **2019**, *7* (20), 6034–6040. https://doi.org/10.1039/c9tc01416k.

(17) Siebert, J. P.; Patarakun, K.; Birkel, C. S. Mechanistic Insights into the Nonconventional Sol-Gel Synthesis of MAX Phase M_2GeC (M = V, Cr). *Inorg Chem* **2022**, *61* (3), 1603–1610. https://doi.org/10.1021/acs.inorgchem.1c03415.

(18) Siebert, J. P.; Juelsholt, M.; Günzing, D.; Wende, H.; Ollefs, K.; Birkel, C. S. Towards a Mechanistic Understanding of the Sol-Gel Syntheses of Ternary Carbides. *Inorg Chem Front* **2022**, *9* (7), 1565–1574. https://doi.org/10.1039/d2qi00053a.

(19) Siebert, J. P.; Hajra, D.; Tongay, S.; Birkel, C. S. The Synthesis and Electrical Transport Properties of Carbon/Cr_2GaC MAX Phase Composite Microwires. *Nanoscale* **2022**, *14* (3), 744–751. https://doi.org/10.1039/d1nr06780j.

(20) Siebert, J. P.; Mallett, S.; Juelsholt, M.; Pazniak, H.; Wiedwald, U.; Page, K.; Birkel, C. S. Structure Determination and Magnetic Properties of the Mn-Doped MAX Phase Cr_2GaC. *Mater Chem Front* **2021**, *5* (16), 6082–6091. https://doi.org/10.1039/d1qm00454a.

(21) Sinclair, J.; Siebert, J. P.; Juelsholt, M.; Shen, C.; Zhang, H.; Birkel, C. S. Sol Gel-Based Synthesis of the Phosphorus-Containing MAX Phase V_2PC. *Inorg Chem* **2022**, *61* (43), 16976–16980. https://doi.org/10.1021/acs.inorgchem.2c02880.

(22) Kubitza, N.; Reitz, A.; Zieschang, A. M.; Pazniak, H.; Albert, B.; Kalha, C.; Schlueter, C.; Regoutz, A.; Wiedwald, U.; Birkel, C. S. From MAX Phase Carbides to Nitrides: Synthesis of V_2GaC, V_2GaN, and the Carbonitride $V_2GaC_{1-X}N_x$. *Inorg*

Chem **2022**, *61* (28), 10634–10641. https://doi.org/10.1021/acs.inorgchem.2c00200.

(23) Siebert, J. P.; Flores, M.; Birkel, C. S. Shape Control of MAX Phases by Biopolymer Sol–Gel Synthesis: Cr_2GaC Thick Films, Microspheres, and Hollow Microspheres. *ACS Organic & Inorganic Au* **2022**, *2* (1), 59–65. https://doi.org/10.1021/acsorginorgau.1c00022.

(24) C-P-V Isothermal Section of Ternary Phase Diagram: Datasheet from "PAULING FILE Multinaries Edition – 2022" in SpringerMaterials (Https://Materials.Springer.Com/Isp/Phase-Diagram/Docs/C_0955465). Springer-Verlag Berlin Heidelberg & Material Phases Data System (MPDS), Switzerland & National Institute for Materials Science (NIMS), Japan. https://materials.springer.com/isp/phase-diagram/docs/c_0955465.

(25) Silversmit, G.; Depla, D.; Poelman, H.; Marin, G. B.; De Gryse, R. Determination of the V2p XPS Binding Energies for Different Vanadium Oxidation States (V^{5+} to V^{0+}). *J Electron Spectros Relat Phenomena* **2004**, *135* (2–3), 167–175. https://doi.org/10.1016/j.elspec.2004.03.004.

(26) Sydorchuk, V.; Zazhigalov, V.; Khalameida, S.; Diyuk, E.; Skubiszewska-Ziba, J.; Leboda, R.; Kuznetsova, L. Solvothermal Synthesis of Vanadium Phosphates in the Form of Xerogels, Aerogels and Mesostructures. *Mater Res Bull* **2010**, *45* (9), 1096–1105. https://doi.org/10.1016/j.materresbull.2010.06.010.

(27) Park, J.; Ahn, K.; Yu, S.; An, J.; Lee, T. H.; Kim, M. G. Oxidation State Control of Solution-Processed Vanadium Oxide Thin-Films and Resistive Switching of VO_2 Thin-Film in a Metastable State. *Thin Solid Films* **2018**, *648* (December 2017), 69–75. https://doi.org/10.1016/j.tsf.2017.12.024.

(28) Weil, J. A.; Bolton, J. R. *Electron Paramagnetic Resonance: Elementary Theory and Practical Applications*; Wiley: Hoboken, 2007.

(29) Stoll, S.; Schweiger, A. EasySpin, a Comprehensive Software Package for Spectral Simulation and Analysis in EPR. *Journal of Magnetic Resonance* **2006**, *178* (1), 42–55. https://doi.org/10.1016/j.jmr.2005.08.013.

(30) Schlueter, C.; Gloskovskii, A.; Ederer, K.; Schostak, I.; Piec, S.; Sarkar, I.; Matveyev, Y.; Lömker, P.; Sing, M.; Claessen, R.; Wiemann, C.; Schneider, C. M.; Medjanik, K.; Schönhense, G.; Amann, P.; Nilsson, A.; Drube, W. The New Dedicated HAXPES Beamline P22 at PETRAIII. In *AIP Conference Proceedings*; American Institute of Physics Inc., 2019; Vol. 2054. https://doi.org/10.1063/1.5084611.

(31) Coelho, A. A. TOPAS and TOPAS-Academic: An Optimization Program Integrating Computer Algebra and Crystallographic Objects Written in C++: An. *J Appl Crystallogr* **2018**, *51* (1), 210–218. https://doi.org/10.1107/S1600576718000183.

(32) Juhás, P.; Davis, T.; Farrow, C. L.; Billinge, S. J. L. PDFgetX3: A Rapid and Highly Automatable Program for Processing Powder Diffraction Data into Total Scattering Pair Distribution Functions. *J Appl Crystallogr* **2013**, *46* (2), 560–566. https://doi.org/10.1107/S0021889813005190.

(33) Yang, X.; Juhas, P.; Farrow, C. L.; Billinge, S. J. L. XPDFsuite: An End-to-End Software Solution for High Throughput Pair Distribution Function Transformation, Visualization and Analysis. **2014**, 1–4.

(34) Farrow, C. L.; Juhas, P.; Liu, J. W.; Bryndin, D.; Boin, E. S.; Bloch, J.; Proffen, T.; Billinge, S. J. L. PDFfit2 and PDFgui: Computer Programs for Studying

Nanostructure in Crystals. *Journal of Physics Condensed Matter* **2007**, *19* (33). https://doi.org/10.1088/0953-8984/19/33/335219.

(35) Dai, H.; Zhao, H.; Chen, S.; Jiang, B. A Microwave-Assisted Boudouard Reaction: A Highly Effective Reduction of the Greenhouse Gas CO_2 to Useful Co Feedstock with Semi-Coke. *Molecules* **2021**, *26* (6). https://doi.org/10.3390/molecules26061507.

(36) Krzystek, J.; Ozarowski, A.; Telser, J.; Crans, D. C. High-Frequency and -Field Electron Paramagnetic Resonance of Vanadium (IV, III, and II) Complexes. *Coordination Chemistry Reviews*. Elsevier October 15, 2015, pp 123–133. https://doi.org/10.1016/j.ccr.2014.10.014.

(37) Quackenbush, N. F.; Paik, H.; Woicik, J. C.; Arena, D. A.; Schlom, D. G.; Piper, L. F. J. X-Ray Spectroscopy of Ultra-Thin Oxide/Oxide Heteroepitaxial Films: A Case Study of Single-Nanometer VO_2/TiO_2. *Materials* **2015**, *8* (8), 5452–5466. https://doi.org/10.3390/ma8085255.

(38) Basso, M.; Colusso, E.; Carraro, C.; Kalha, C.; Riaz, A. A.; Bombardelli, G.; Napolitani, E.; Chen, Y.; Jasieniak, J.; Ratcliff, L. E.; Thakur, P. K.; Lee, T. L.; Regoutz, A.; Martucci, A. Rapid Laser-Induced Low Temperature Crystallization of Thermochromic VO_2 Sol-Gel Thin Films. *Appl Surf Sci* **2023**, *631* (May), 157507. https://doi.org/10.1016/j.apsusc.2023.157507.

(39) Tanuma, S.; Powell, C. J. Electron Inelastic Mean Free Paths. 5. Data for 14 Organic-Compunds over the 50-2000 EV Range. *Surface and Interface Analysis* **1994**, *21* (September 1993), 165–176.

(40) De Luna, Y.; Bensalah, N. Synthesis, Characterization and Electrochemical Evaluation of Layered Vanadium Phosphates as Cathode Material for Aqueous Rechargeable Zn-Ion Batteries. *Front Mater* **2021**, *8*. https://doi.org/10.3389/fmats.2021.645915.

(41) Coates, J. Interpretation of Infrared Spectra, A Practical Approach. *Encyclopedia of Analytical Chemistry* **2006**, 1–23. https://doi.org/10.1002/9780470027318.a5606.

(42) Liu, L.; Wang, X.; Bontchev, R.; Ross, K.; J. Jacobson, A. Influence of Reaction Conditions on the Electrochemical-Hydrothermal Synthesis of Two Ammonium Vanadium Phosphates: $(NH_4)_2VO(HPO_4)2{\cdot}H2O$ and $(NH_4)_2VO(V_{0.88}P_{1.12}O_7)$. *J Mater Chem* **1999**, *9* (7), 1585–1589. https://doi.org/10.1039/A901956A.

(43) Jastrzbski, W.; Sitarz, M.; Rokita, M.; Bułat, K. Infrared Spectroscopy of Different Phosphates Structures. *Spectrochim Acta A Mol Biomol Spectrosc* **2011**, *79* (4), 722–727. https://doi.org/10.1016/j.saa.2010.08.044.

For Table of Contents Only

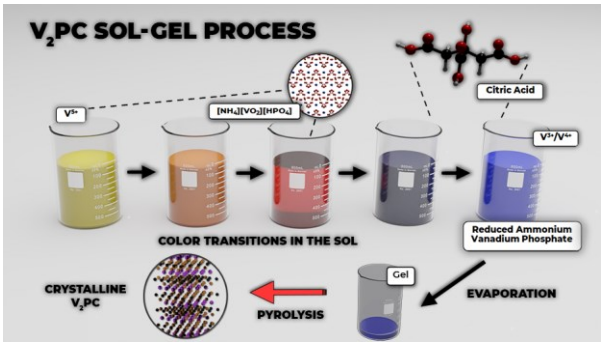

MAX phase V_2PC can be prepared by sol gel-assisted method involving metal salts and citric acid that acts as a gelling agent and carbon source. We unravel the intermediate species and chemical reactions that occur throughout the entire process (between room temperature and 950 C) by combining spectroscopy, diffraction and thermal analysis techniques. Insights into the chemistries during this synthesis approach may guide the synthesis of further MAX phases or similar P-containing compounds.